Title
Representation of sharp rifts and faults mechanics in modeling ice shelf flow dynamics: Application to Brunt/Stancomb-Wills Ice Shelf, Antarctica

Journal
Journal of Geophysical Research Earth Surface, 119(9)

ISSN
2169-9003

Authors
Larour, E
Khazendar, A
Borstad, CP
et al.

Publication Date
2014-09-01

DOI
10.1002/2014jf003157

AGU PUBLICATIONS

JGR

Journal of Geophysical Research: Earth Surface

RESEARCH ARTICLE

10.1002/2014JF003157

Key Points:
- New ice flow model that better captures the state of contact/friction of cracks
- New data assimilation of ice rheology that takes into account faults and rifts
- New understanding of how friction controls the dynamic stability of ice shelves

Correspondence to:
E. Larour,
Eric.Larour@jpl.nasa.gov

Citation:
Larour, E., A. Khazendar, C. P. Borstad, H. Seroussi, M. Morlighem, and E. Rignot (2014), Representation of sharp rifts and faults mechanics in modeling ice shelf flow dynamics: Application to Brunt/Stancomb-Wills Ice Shelf, Antarctica, *J. Geophys. Res. Earth Surf.*, *119*, 1918–1935, doi:10.1002/2014JF003157.

Received 27 MAR 2014
Accepted 16 AUG 2014
Accepted article online 21 AUG 2014
Published online 22 SEP 2014

Representation of sharp rifts and faults mechanics in modeling ice shelf flow dynamics: Application to Brunt/Stancomb-Wills Ice Shelf, Antarctica

E. Larour[1], A. Khazendar[1], C. P. Borstad[2], H. Seroussi[1], M. Morlighem[3], and E. Rignot[1,3]

[1] Jet Propulsion Laboratory, California Institute of Technology, Pasadena, California, USA, [2]California Institute of Technology, Pasadena, California, USA, [3]Department of Earth System Science, University of California, Irvine, California, USA

Abstract Ice shelves play a major role in buttressing ice sheet flow into the ocean, hence the importance of accurate numerical modeling of their stress regime. Commonly used ice flow models assume a continuous medium and are therefore complicated by the presence of rupture features (crevasses, rifts, and faults) that significantly affect the overall flow patterns. Here we apply contact mechanics and penalty methods to develop a new ice shelf flow model that captures the impact of rifts and faults on the rheology and stress distribution of ice shelves. The model achieves a best fit solution to satellite observations of ice shelf velocities to infer the following: (1) a spatial distribution of contact and friction points along detected faults and rifts, (2) a more realistic spatial pattern of ice shelf rheology, and (3) a better representation of the stress balance in the immediate vicinity of faults and rifts. Thus, applying the model to the Brunt/Stancomb-Wills Ice Shelf, Antarctica, we quantify the state of friction inside faults and the opening rates of rifts and obtain an ice shelf rheology that remains relatively constant everywhere else on the ice shelf. We further demonstrate that better stress representation has widespread application in examining aspects affecting ice shelf structure and dynamics including the extent of ice mélange in rifts and the change in fracture configurations. All are major applications for better insight into the important question of ice shelf stability.

1. Introduction

The disintegration of ice shelves in the Antarctic Peninsula in the past two decades has focused attention on the role of ice shelves in stabilizing the Antarctic Ice Sheet. Indeed, following the partial collapse of the Wilkins Ice Shelf from 1998 to 2009, the disintegration of the Larsen A Ice Shelf in 1995 and the disintegration of the Larsen B Ice Shelf in 2002, tributary glaciers feeding each of these ice shelves underwent sustained accelerations [*Rott et al.*, 2002; *De Angelis and Skvarca*, 2003; *Scambos et al.*, 2004; *Rignot et al.*, 2004; *Pritchard and Vaughan*, 2007; *Hulbe et al.*, 2008]. This resulted in increased mass fluxes at the grounding line, leading to increased contributions to sea level rise [*Rignot et al.*, 2005; *Pritchard and Vaughan*, 2007]. Several factors are cited as contributing to the collapse of these ice shelves, among them climatic forcing resulting in increased surface melting [*van den Broeke*, 2005] and melt water ponding leading to fracturing of the ice shelf prior to collapse [*Scambos et al.*, 2000, 2009; *Banwell et al.*, 2013]. Other scenarios involve increased fracturing of the suture zones and the weakening of ice mélange inside rifts that penetrate the entire thickness of the ice shelf [*Khazendar et al.*, 2007, 2009], this weakening possibly being of oceanic origin [*Shepherd et al.*, 2003]; and the ice-shelf-fragment-capsize mechanism [*MacAyeal et al.*, 2003]. Irrespective of the relative contribution of each of these processes, fracturing plays a central role in determining the stability of ice shelves.

Historically, most studies have focused on explaining fracturing of ice shelves using crack initiation criteria based on the background longitudinal stress or strain rate such as in *Vaughan* [1993]. Once an initial crack develops at the surface, a simple stress balance analysis shows that the crack will propagate downward due to the stress imbalance between the background horizontal longitudinal stress, the vertical lithostatic stress, and the hydrostatic water pressure [*Weertman*, 1973; *Smith*, 1976]. Such crevasses sometimes reach the bottom of the ice shelf, forming vertical rifts that will propagate sideways across the ice shelf. Similar analysis by *Weertman* [1980] showed that bottom crevasses can also form, requiring a much lower background longitudinal stress in order to develop and propagate upward, due to the significantly higher water pressure at the ice/ocean interface. More recently, this type of analysis has been revisited using Linear Elastic Fracture

Mechanics (LEFM) in order to better understand the impact of stress on crack initiation and propagation [*van der Veen*, 1998; *Rist et al.*, 1999; *Plate et al.*, 2012]. Background stress is a result of the creeping of ice under its own weight and is therefore difficult to reconcile with an elastic stress regime near the rupture tip. Nevertheless, observations [*Fricker et al.*, 2005; *Bassis et al.*, 2005, 2007, 2008] do indeed hint at a direct link between background stress and elastic crack propagation, which suggests that the stress balance of an ice shelf undergoing creep deformation fully describes the loading conditions under which a crack will propagate. Models such as *Larour et al.* [2004] and *Hulbe et al.* [2010] have worked under this assumption to study how fractures propagate laterally in a given background glaciological stress field.

The impact of the presence of rifts and faults on the background stress itself is not, however, fully understood. Recently, efforts at understanding this impact have been directed at a better description of how ice rheology and dynamics are influenced by fracturing of the ice and how weakening of the ice can destabilize the overall ice flow and stress regime of the ice shelf [*MacAyeal*, 1989; *MacAyeal et al.*, 1998; *Larour et al.*, 2005; *Vieli et al.*, 2006; *Khazendar et al.*, 2007, 2009; *Humbert et al.*, 2009; *Borstad et al.*, 2012]. *MacAyeal* [1989], for example, suggests that the presence of faults at margins of the Ross Ice Shelf is responsible for a shear stress transmission lower than previously thought. That model introduces Coulomb friction along faults at the boundaries and accounts for the impact of such faulting on the overall background stress. However, the *MacAyeal* [1989] study does not introduce rifts across the ice shelf itself. Another important example is the role of ice mélange in rifts. The mélange can act as a stabilizer by transmitting stresses between flanks of the rift [*MacAyeal et al.*, 1998; *Larour et al.*, 2004; *Borstad et al.*, 2013], which will significantly impact the overall stress balance of the ice shelf. In addition, the sensitivity of the ice mélange to atmospheric and oceanic conditions introduces a link between climate variability, ocean circulation, and ice flow dynamics, which needs to be accounted for. As suggested in *Larour et al.* [2004] and *Bassis et al.* [2007], the composition of this mélange, as well as its thermodynamical state and rheology, are also critical in controlling the evolution of rifts, which again underscores the need to improve our understanding of how the presence of rifts impacts ice flow dynamics.

Here we aim to address the misrepresentation of ice rheology and fracture in ice flow modeling that relies on inverse methods to constrain ice rigidity and to understand the impact a better representation of these two related elements will have on the overall stress balance and ice flow dynamics. Ice rheology is often described using a nonlinear viscous relationship between effective stress and strain rate, based on Glen's flow law [*Glen*, 1955]. This relationship depends mainly on ice rigidity, a strain rate independent parameter that depends on ice temperature, ice fabrics, and pressure among others [*Paterson*, 1994]. The complexity of this parameter is such that inverse methods using surface velocity observations are sometimes relied upon to characterize its highly variable magnitude and spatial distribution [*MacAyeal et al.*, 1998; *Larour*, 2005; *Vieli et al.*, 2006, 2007; *Khazendar et al.*, 2007, 2009, 2011]. Such methods assume a continuous medium to invert for the ice rigidity. In some areas, however, fracture can occur where ice will rupture through the entire thickness of the ice. We refer to this type of fracture as a rift (if it is opening), or a fault (if both flanks of the column of ice are in contact). Where this fracturing occurs, the basic assumption of a continuum medium is no longer valid, and inverse methods tend to accommodate for these ruptures by generating areas of artificially low ice shelf rigidity, e.g., within a rift or a fault, or areas of rapidly varying ice shelf rigidity, e.g., across a rupture zone [*Khazendar et al.*, 2009]. Such results suggest that inversions no longer accurately capture the actual physical properties of the ice in the latter areas. In addition, the overall stress balance modeled by the inversion across an ice shelf is no longer realistic. Approaches such as damage mechanics have tried and bridge the gap between the need for a continuum representation of stress balance and the inherent discontinuous nature of cracks. These approaches consist in multiplying the ice viscosity by $(1 - D)$ where D is a damage variable that varies between 0 (fully crack) to 1 (fully load-bearing ice) [*Borstad et al.*, 2012]. Inversions of the ice rigidity and damage are equivalent as the two variables B and D have the same effect on the ice viscosity. Such approaches are diffuse in nature, because they model a discontinuous crack as a continuous weakening of the ice rheology (or corresponding increase in ice damage). They are therefore mesh dependent, as the spatial scale over which the weakening occurs cannot be less than the minimum mesh element size.

Here we present a new ice flow model that captures the impact of rifts and faults on stress balance using the theory of contact mechanics [*Wriggers*, 2002] and penalty methods [*Courant*, 1943]. We do not attempt to model the propagation or initiation of such cracks, nor model the elastic response of the ice shelf. Indeed, this is best done using an LEFM framework. Our model is instead used to invert for the rigidity of the

Brunt/Stancomb-Wills Ice Shelf system (BSW), Antarctica, where the presence of a large number of rifts and faults has been shown by *Khazendar et al.* [2009] to have a determinant influence on ice flow and ice shelf rheology. We discuss how the new model is able to identify rift and fault zones and to quantify the stress regime and ice rheology make up of these regions in a mesh-independent way. We conclude by a discussion of the impact of our new findings on the study of the mechanical and dynamic stability of ice shelves, specifically as it relates to oceanic circulation and the thickness of the ice mélange present inside rifts and faults.

2. Model

2.1. Equations

The model is based on the two dimensional (2-D) MacAyeal implementation [*MacAyeal*, 1989, 1992] of the Shallow Shelf Approximation (SSA). The equations of ice flow, expressed in terms of (u, v), the depth-averaged horizontal velocity, are as follows:

$$\frac{\partial}{\partial x}\left(4H\bar{\mu}\frac{\partial u}{\partial x}+2H\bar{\mu}\frac{\partial v}{\partial y}\right)+\frac{\partial}{\partial y}\left(H\bar{\mu}\frac{\partial u}{\partial y}+H\bar{\mu}\frac{\partial v}{\partial x}\right)=\rho g H\frac{\partial s}{\partial x} \tag{1}$$

$$\frac{\partial}{\partial y}\left(4H\bar{\mu}\frac{\partial v}{\partial y}+2H\bar{\mu}\frac{\partial u}{\partial x}\right)+\frac{\partial}{\partial x}\left(H\bar{\mu}\frac{\partial u}{\partial y}+H\bar{\mu}\frac{\partial v}{\partial x}\right)=\rho g H\frac{\partial s}{\partial y} \tag{2}$$

where (x, y) are the horizontal coordinates, H is the local ice thickness, $\bar{\mu}$ the depth-averaged ice viscosity, ρ the ice density, g the acceleration due to gravity, and s the upper surface elevation of the ice.

Equations (1) and (2) express the horizontal balance of stresses, assuming that (1) the ice flow acceleration is negligible [*Reist*, 2005]; (2) vertical shear is negligible, and (3) ice is incompressible. These three assumptions are mostly valid for the case of an ice shelf.

The SSA model also requires a material constitutive law, which describes the deformation of ice under stress. For incompressible viscous fluids, the constitutive law is as follows:

$$\boldsymbol{\sigma}' = 2\mu\dot{\boldsymbol{\epsilon}} \tag{3}$$

where $\boldsymbol{\sigma}' = \boldsymbol{\sigma} + p\mathbf{I}$ is the deviatoric stress tensor, $\mathbf{I}$ the identity matrix, p the ice pressure, and μ the ice effective viscosity. The ice effective viscosity is assumed to be nonlinear and to follow a Norton-Hoff law [*Glen*, 1955]:

$$\mu = \frac{B}{2\,\dot{\epsilon}_e^{\frac{n-1}{n}}} \tag{4}$$

where B is the ice rigidity, n Glen's law exponent, and $\dot{\epsilon}_e$ the effective strain rate (defined as the second invariant of the strain rate tensor). Equation (4) can be depth integrated, to yield a similar relationship in which μ is replaced by $\bar{\mu}$ and B is replaced by $\bar{B}$, the depth-averaged ice rigidity. $\bar{B}$ is temperature and fabric dependent and is considered a material parameter in our study, which will be inverted for using an adjoint-based inversion.

The model boundary conditions are described as follows: (1) at the grounding line, kinematic constraints are applied, where the velocity is set to the observed surface velocity; (2) at the ice front, water pressure is imposed according to

$$\begin{aligned} \boldsymbol{\sigma}\cdot\mathbf{n} &= \rho_w g z\,\mathbf{n} \quad \text{for } z<0 \\ \boldsymbol{\sigma}\cdot\mathbf{n} &= \mathbf{0} \qquad\quad \text{for } z\geq 0 \end{aligned} \tag{5}$$

where ρ_w is the water density, $\mathbf{n}$ the normal to the ice front, and z the vertical coordinate equal to zero at sea level (positive upward). This boundary condition can be depth integrated to yield a formulation compatible with equations (1) and (2) [*Morland and Zainuddin*, 1987]:

$$\int_b^s \sigma_{nn}\mathrm{d}z = -\frac{1}{2}\rho_w g b^2 \tag{6}$$

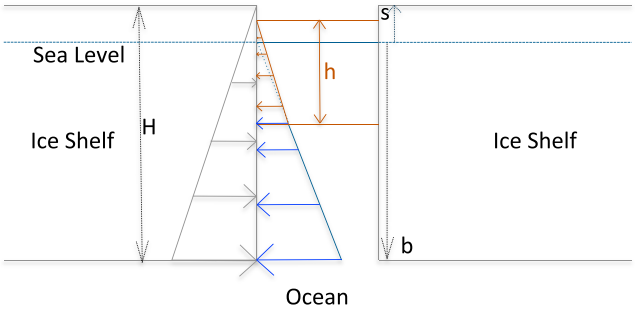

Figure 1. Cross section of a rifted ice shelf. Ice mélange of thickness *h* fills the rift (in brown). Sea level is marked in blue and represents the 0 level of the vertical axis, *s* the ice shelf height above sea level, *H* its ice thickness, and *b* the ice shelf draft. Pressure distributions along the left flank of the rift are indicated by arrows (gray for the lithostatic ice pressure, brown for the ice mélange pressure, and blue for the water pressure).

where σ_{nn} is the normal stress to the ice front, *b* and *s* the elevation of the lower and upper surface of the ice shelf above mean sea level.

Equations (1), (2), (4), and (6) represent a complete system of equations for the case of a nonfractured ice shelf flowing under its own weight. If the ice is fractured over the entire ice thickness, which is the case when faults or rifts are present, a different approach is required. Here we model these fractures by introducing through-thickness cracks of zero width in the model domain. These geometrical discontinuities introduce new boundary conditions and additional velocity constraints.

In the case of a rift, the flanks of the crack are apart, leaving space within the fracture which will fill with open water and ice mélange. The boundary conditions for such a scenario can be inferred in a similar way to that of an ice front (Figure 1). There is no shearing between flanks (as they are not in contact), and the normal stress, σ_{nn}, equals the combined air (negligible), water, and mélange pressure. Integrated over the entire ice thickness, this results in

$$\int_b^s \sigma_{nn} \mathrm{d}z = -\frac{\rho_i g (\alpha H)^2}{2} - \frac{\rho_w g}{2}\left[b^2 - \left(\frac{\rho_i}{\rho_w}\alpha H\right)^2\right] \tag{7}$$

where α is the mélange volume fraction (ratio between ice mélange thickness *h* and local ice shelf thickness *H*). The first term on the right-hand side of equation (7) corresponds to the mélange contribution and the second to the water contribution. This set of boundary conditions assumes that the mélange within a rift is not a continuous medium in which stresses are transmitted from one flank to the other. This may not be entirely correct, as evidenced by work from *Rignot* [1998] and *Larour et al.* [2005], which suggest that mélange within rifts is mechanically coherent when sufficiently thick. However, capturing shear stresses within the ice mélange would involve a considerably more complex model, assuming a rheology could be inferred for the mélange. Here we restrict ourselves to a scenario where mélange is modeled as an outside constraint on the ice shelf system, i.e., as an additional set of boundary conditions on the rift flanks and not as a part of the geometrical domain where ice velocity is solved for. This also implies that the mélange inside rifts is not capable of transmitting tensile stresses, just compressive and shearing stresses.

In the case of a fault, the Penalty Method [*Courant*, 1943] is used to enforce a non-interpenetration condition, where normal velocities v_{n1} and v_{n2} across flanks of a fault are made equal. This is achieved by adding to the normal stress σ_{nn} an arbitrarily large component proportional to the difference $v_{n1} - v_{n2}$, i.e.,

$$\sigma_{nn} = \lambda\left(v_{n1} - v_{n2}\right) \tag{8}$$

where λ is a penalty factor. If λ is chosen large enough, both normal velocities will be equal. If such a condition is ensured for all contact locations distributed along the flanks of the fault, this will essentially ensure a condition of non-interpenetration of both flanks. Equation (8) can be depth averaged by multiplying by the thickness *H*, but we choose to lump this multiplier within λ itself, without loss of generality.

Once contact occurs, and non-interpenetration of both flanks is ensured, shearing between both flanks can be modeled. The shearing is mainly lateral, along the crack axis, given that vertical shearing is negligible for ice shelves, even when tidally induced [*Larour*, 2005]. This is modeled using a viscous shear resistance, where σ_{nt}, the lateral shear along the fault, is proportional to the difference in tangential velocities v_{t1} and v_{t2} across flanks. If this relationship is depth averaged, we get

$$\sigma_{nt} = \nu H\left(v_{t1} - v_{t2}\right) \tag{9}$$

where ν is the viscous friction coefficient, taken constant both in time and for each fault.

A fundamental aspect of our model is that contact locations within cracks do not need to be predetermined, but are rather computed by the ice flow model. This is not to be confused with the position of the crack itself, which is not computed, but must be defined within the geometrical domain itself before running the model. For a given velocity field, normal penetration at each crack segment is calculated as follows: if penetration is positive (flanks are in contact), contact penalties are activated to ensure non-penetration, and a new velocity field is calculated. If penetration is negative (flanks are opening), boundary conditions in equation (7) are applied and penalty conditions are relaxed. This iterative process is carried forward until a convergence is achieved to a stable solution. In effect, what this new model captures is a steady state of contact for all chosen cracks of an ice shelf, which is compatible with the steady state equations for the SSA model. One of the model outputs is therefore the spatial distribution of the state of contact for all cracks, i.e., whether a crack is opening (for a rift) or closed (for a fault). Indeed, we believe this is a unique feature of this model, as it computes not only the depth-averaged velocity field but also the stress distribution of cracks and their corresponding state.

2.2. Discretization

Equations (1), (2), (4), (6), and (7) are solved using the continuous Galerkin finite element method (FEM), which we implement using the Ice Sheet System Model (ISSM) framework [*Larour et al.*, 2012; *Morlighem et al.*, 2010].

To discretize equation (8) using the FEM, we add to the global stiffness matrix K generated for equations (1) and (2), a new stiffness matrix, K_{ij}, between degrees of freedom (V_x and V_y), where V_x is the velocity along the x axis of the fracture and V_y along the y axis of the fracture, of locations i and j which are in contact, such that it penalizes any difference in normal velocity between the two vertices. K_{ij} is expressed as follows [*Wriggers*, 2002]:

$$K_{ij} = \lambda \begin{bmatrix} n_x^2 & n_x n_y & -n_x^2 & -n_x n_y \\ n_x n_y & n_y^2 & -n_x n_y & -n_y^2 \\ -n_x^2 & -n_x n_y & n_x^2 & n_x n_y \\ -n_x n_y & -n_y^2 & n_x n_y & n_y^2 \end{bmatrix} \tag{10}$$

where $\mathbf{n} = (n_x, n_y)$ is the local normal to the crack and λ the penalty coefficient. The ordering of the degrees of freedom for locations i and j is as follows: V_{xi}, V_{yi}, V_{xj}, and V_{yj}. If λ is chosen much greater than the stiffness matrix norm $|K|$, then this method will ensure that normal velocities of vertices i and j are identical.

For the tangential shear expressed in equation (9), we similarly discretize it using an additional stiffness K'_{ij} between vertices i and j, such that, following [*Wriggers*, 2002]:

$$K'_{ij} = \nu H l \begin{bmatrix} n_y^2 & -n_x n_y & -n_y^2 & n_x n_y \\ -n_x n_y & n_x^2 & n_x n_y & -n_x^2 \\ -n_y^2 & n_x n_y & n_y^2 & -n_x n_y \\ n_x n_y & -n_x^2 & -n_x n_y & n_x^2 \end{bmatrix} \tag{11}$$

where l is the length of the mesh segment to which vertices i and j belong.

2.3. Stabilization

To reach a steady state ice flow model where the state of contact is stabilized (i.e., each segment of the ice shelf cracks is stable, with a defined state of stress and contact), the ice flow model needs to be iterated upon. However, convergence can be difficult to achieve because of numerical zigzagging or wiggling [*Wriggers*, 2002] between a state of opening and closing for each crack segment. The reason for this zigzagging is the fact that the transition from a boundary condition of contact, where the normal stress is equal to the lithostatic stress (equation (7) with $\alpha = 1$), to a boundary condition of open water (equation (7) with $\alpha = 0$) is very abrupt and not captured at the right time scale by the model. Indeed, a rift cannot open instantaneously, and elastic deformation is bound to occur. In addition, mélange will fall within the rift, creating an initial mélange thickness that is not 0. Therefore, an iterative process is necessary to converge toward a state where rifts are filled with open water and a small amount of mélange. In this process, α is initially set to 0 for all segments of the ice shelf cracks, and as zigzagging develops for certain segments, α is gradually increased until the zigzagging stops. The overall result is a model where zigzagging is stabilized and where a realistic boundary condition is computed for time scales that are relevant to a viscous deformation regime, along with mélange thicknesses that corresponds to a situation of stable stress balance.

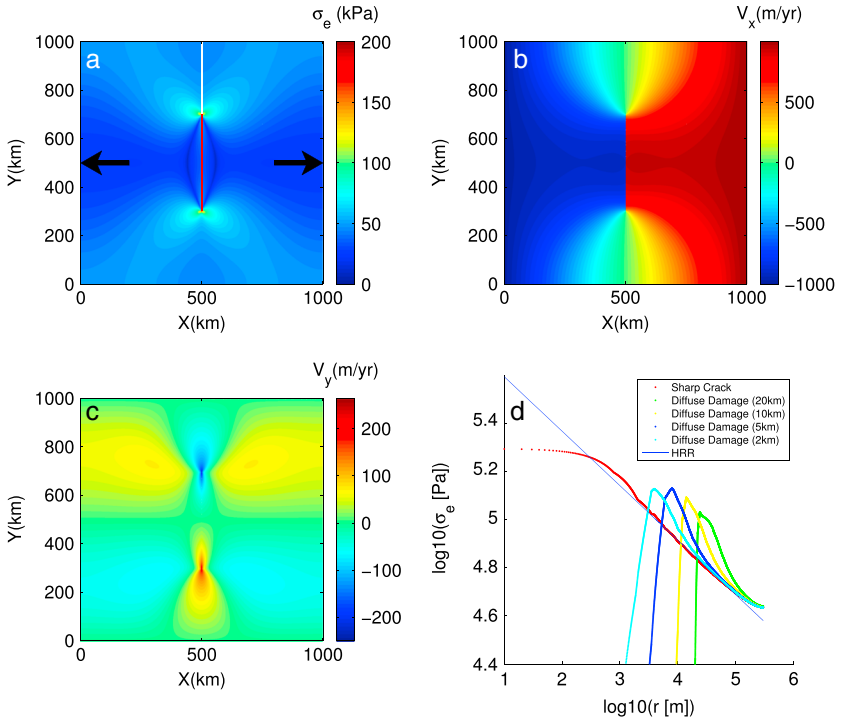

Figure 2. Model of a synthetic square ice shelf cracked in the middle over 500 km. Both lateral boundaries ($y = 0$ and $y = 1000$ km) experience free slip conditions, and inflow and outflow velocities (at $x = 0$ km and $x = 1000$ km, respectively) are set to −1000 m/yr and 1000 m/yr, respectively. (a) Effective stress σ_e in kPa. The crack is indicated by the red line. The white dashed line is used to validate against analytical results in Figure 2d. (b and c) V_x and V_y in m/yr. (d) Comparison between modeled effective stress σ_e (in red) and theoretical HRR (Hutchinson, Rice, and Rosengren) [from *Hutchinson*, 1968; *Rice and Rosengren*, 1968] stress singularity (blue line), along the white dashed profile defined in Figure 2a. Scale is logarithmic both in σ_e and r (where r is the distance from the crack tip along the white dashed profile in Figure 2a). For reference, we also include the effective stress for an identical configuration where the crack is simulated by a band of zero rigidity $B = 10$ kPa.yr$^{1/3}$ (a value of 0 would trigger singularity in the stiffness matrix, which is why we leave a small residual of 10 kPa.yr$^{1/3}$) of width 20 km (green), 10 km (yellow), 5 km (blue), and 2 km (cyan), respectively.

2.4. Inversion

Following *Larour et al.* [2004], *Morlighem et al.* [2010], and *Larour et al.* [2012], an adjoint-based inversion capability was also developed for the new ice flow model. This capability allows for the inversion of ice rigidity B given observed surface velocities, assuming a linearization of equation (4) where the strain rate is considered constant and given in addition an equivalent solid ice thickness from surface elevation measurements corrected for the thickness and density of the firn layer. The adjoint computation is straightforward, equation (7) being independent of ice velocity, and equations (8) and (9) being linear with respect to ice velocity. The computation of the gradient of the misfit between model and surface velocity with respect to ice rigidity B is also straightforward, all boundary conditions in equations (7), (8), and (9) being independent of B itself. The algorithm itself for the inversion is identical to *Larour et al.* [2004] and *Morlighem et al.* [2010] and is explained in detail in *Larour et al.* [2012].

3. Validation

Tests are run to validate the new ice flow model in its capacity to capture the presence of rifts and faults in an ice shelf. All tests are run on an idealized square ice shelf 1000 km × 1000 km in size, 300 m in thickness, cracked at its center over a length of 500 km and over the entire depth of the ice, and constrained to zero normal velocities laterally ($y = 0$ and $y = 1000$ km) (Figure 2). In order to simulate the presence of a rift, and to force the fracture to open, velocities of −1000 m/yr at $x = 0$ km and 1000 m/yr at $x = 1000$ km are imposed. As expected, the model captures opening of the crack along the entire length (Figures 2b and 2c), with stress concentrations developing at both rupture tips (Figure 2a). These stress concentrations can easily be validated against the theory of stress singularities for a power law deforming material, also referred to

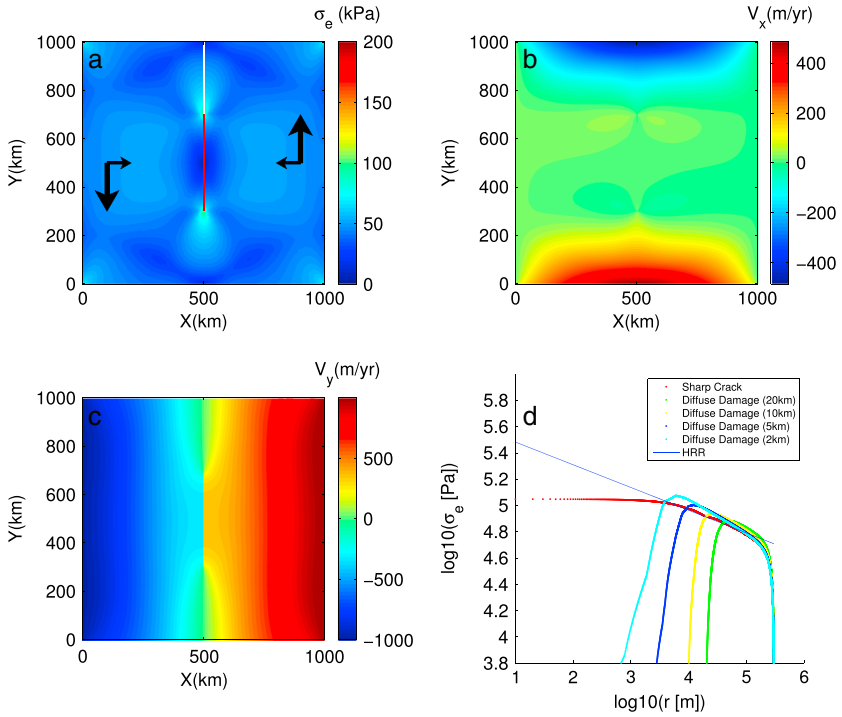

Figure 3. Model of a synthetic square ice shelf cracked in the middle over 500 km. Both lateral boundaries ($y = 0$ and $y = 1000$ km) are free to deform without constraints. The inflow and outflow velocities (at $x = 0$ km and $x = 1000$ km, respectively) are set to $(Vx, Vy) = (100, -1000)$ m/yr and $(Vx, Vy) = (-100, 1000)$ m/yr, respectively. This test case validates the model in shear mode, where the flanks of the rift are in contact (due to compression from the *Vx* boundary condition) and in mode II (shear) deformation (due to the *Vy* boundary condition). (a) Effective stress σ_e in kPa. The crack is indicated by the red line. The white dashed line is used to validate against analytical results in Figure 3d. (b and c) V_x and V_y in m/yr. (d) Comparison between modeled effective stress σ_e (red crosses) and theoretical HRR (Hutchinson, Rice, and Rosengren) [from *Hutchinson*, 1968; *Rice and Rosengren*, 1968] stress singularity (blue line), along the white dashed profile defined in Figure 3a. Scale is logarithmic both in σ_e and r (where r is the distance from the crack tip along the white dashed profile in Figure 3a). For reference, we also include the effective stress for an identical configuration where the crack is simulated by a band of zero rigidity $B = 10$ kPa.yr$^{1/3}$ (a value of 0 would trigger singularity in the stiffness matrix, which is why we leave a small residual of 10 kPa.yr$^{1/3}$) of width 20 km (green), 10 km (yellow), 5 km (blue), and 2 km (cyan), respectively.

as the HRR approximation (Hutchinson, Rice, and Rosengren) [from *Hutchinson*, 1968; *Rice and Rosengren*, 1968]. Indeed, at the rupture tip, the singularity is expected to follow the following relationship:

$$\sigma_e = \frac{K}{r^{1/(n+1)}} f(\theta) \tag{12}$$

where σ_e is the effective stress near the rupture tip, (r, θ) the polar coordinates in the crack axis with origin at the rupture tip, K the fracture toughness in creep mode, and $f(\theta)$ an angular function. The results in Figure 2d) show that the model best fit to the expected HRR stress is reached for a value of the flow law exponent $n = 3.2$, which is 8% different from the expected value of $n = 3$ in Glen's law as applied to ice. This difference is readily explained by the presence of secondary asymptotic expansions of the stress solution in the vicinity of the rupture tip [*Hutchinson*, 1968], and is indeed satisfactory. This demonstrates the capability of the model to correctly capture the creep-mode stress singularity induced by the presence of a rift on an ice shelf. A comparison with the diffuse damage approach where the crack is not modeled by a mesh discontinuity but rather by a band of low rigidity (Figure 2d) shows that the HRR singularity is not replicated correctly, even when considering increasingly smaller bands of low rigidity (widths tested here range from 20 km to 2 km along the crack). By low rigidity, we here imply a rigidity 8 orders of magnitude lower than the background rigidity, which is negligible, but still able to not trigger a singularity in the stiffness matrix of the discretized system of SSA equations. This test demonstrates the need to capture cracks in the ice shelf using the sharp crack approach, at least in the immediate vicinity of the rupture tip (between 3 and 100 km).

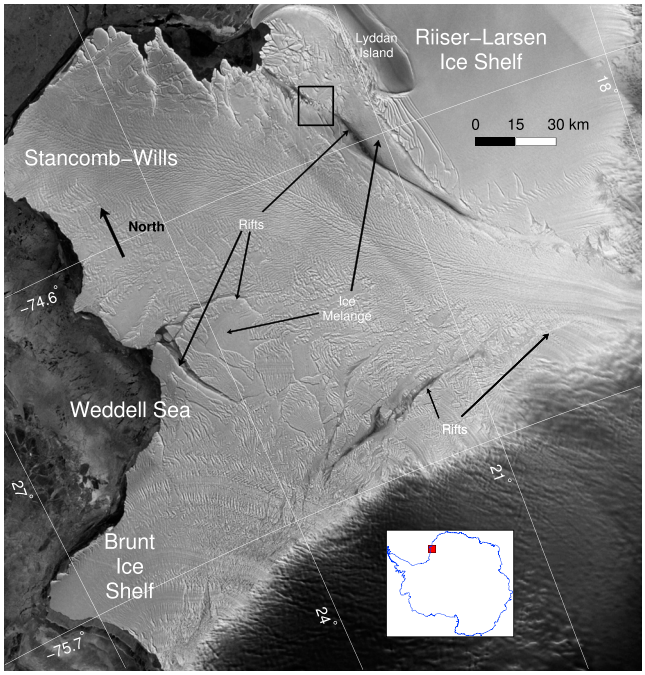

Figure 4. RADARSAT backscatter image of the Brunt/Stancomb-Wills system, taken from the 125 m resolution SAR Mosaic of Antarctica [*Jezek and Team*, 2002]. The data is projected using a Polar Stereographic South projection with central meridian at 0° and standard parallel at −71°. Key rifts/faults are indicated, as well as areas of ice mélange. The "ice bridge" between Stancomb-Wills and Lyddan Island is marked with a black square.

In order to test for the behavior of the model when simulating faults, the same ice shelf configuration is also constrained longitudinally using a compressive rate of 1000 m/yr (results not shown here). The crack indeed acts as a fault, with both flanks remaining in contact. The penalty factor is calibrated using a value 3 orders of magnitude greater than the stiffness norm, to ensure contact penetration of no more than 1 m/yr normal to the crack. Higher values of λ would result in lower penetration rates for faults, which would be more ideal, but higher values of λ would also result in an ill-conditioned equation system for which solvers converge with more difficulty. This choice of λ represents a realistic compromise between the two opposite requirements.

Finally, we carry out shearing tests to calibrate the value of the friction coefficient ν (Figure 3). It is set to 10 kPa yr/m, to account for a shear stress of 100 kPa generated by a tangential velocity differential between both flanks of a fault of 10 m/yr. This value is taken by analogy to results from basal friction inversions at the ice/bed interface [*Morlighem et al.*, 2010; *Larour et al.*, 2012] and is discussed later in the results section. The shearing test exhibits very similar behavior to the tensional test from Figure 2 with respect to the HRR singularity, with a good match to the expected singularity between 1 km and 100 km from the rupture tip. Far from the tip, boundary conditions explain the departure to the HRR singularity, and near the rupture tip, the SSA formulation and mesh resolution are not capable of resolving the stress regime accurately. The same comparison with the diffuse damage approach (Figure 3d) shows a mismatch to the HRR singularity in the same range of distances, further demonstrating the unique ability of our approach to capturing the right stress balance in shear mode.

4. Data and Model Setup

The BSW system (Figure 4) is an ice shelf that exhibits several interesting features that make it an ideal candidate for exploring the impact of the presence of rifts and faults on ice flow dynamics.

First, it has been extensively studied for the past 50–60 years, thanks to the continuous presence of the Halley station on the Brunt Ice Shelf. Consequently, a comprehensive history of its ice flow dynamics as well as climatic and oceanic forcing is available for the past decades [*Thomas*, 1973a; *Simmons and Rouse*, 1984; *Simmons*, 1986; *King*, 1993; *Renfrew and Anderson*, 2002, 2006; *Thoma et al.*, 2006, 2010].

Second, it is located in an area of East Antarctica where the continental shelf is narrow and where the warm Circumpolar Deep Water (CDW) intrudes onto the shelf more easily, resulting in increased melt rates at the ice/ocean boundary [*Thoma et al.*, 2006, 2010]. These melt rates are thought to be critical in controlling the thickness of ice mélange present inside rifts [*Khazendar and Jenkins*, 2003], as well as mélange contributing to the composition of the ice shelf itself. Indeed, the BSW system is made of a complex mix of ice mélange, shelf ice, and icebergs, which react in a cohesive way [*Hulbe et al.*, 2005; *Khazendar et al.*, 2009; *Humbert et al.*, 2009], similar to what was observed and modeled in the Hemmen Ice Rise, Ronne Ice Shelf region by *MacAyeal et al.* [1998], *Rignot* [1998], and *Larour et al.* [2004]. The corresponding pattern of ice rigidity exhibited by this ice shelf [*Khazendar et al.*, 2009] reflects the presence of cold meteoric ice as well as cold air

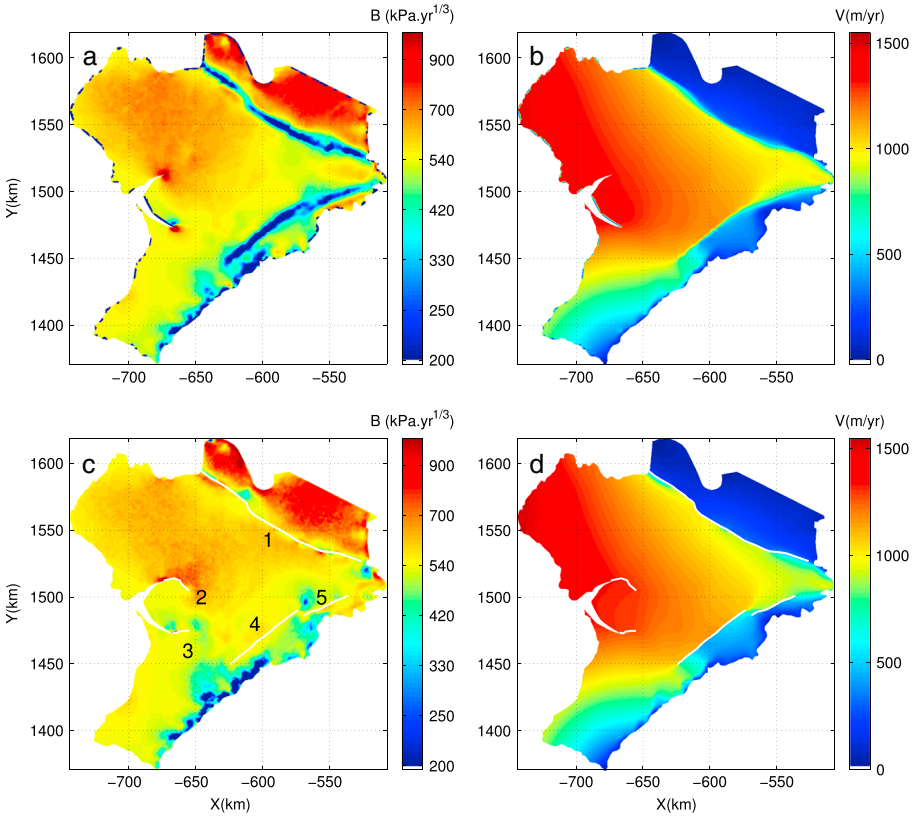

Figure 5. (a) Ice rigidity *B* inferred using an adjoint-based inversion, satellite-derived surface velocities and a forward model where faults and rifts are not represented. (b) Corresponding modeled velocity *V* (m/yr). (c) Ice rigidity *B* inferred using the same derived surface velocities as in Figure 5a and an ice flow model that includes rifts and faults. (d) Corresponding modeled velocity *V* in m/yr. Rifts and faults 1 to 5 are indicated by white lines in Figure 5c.

ponding on the Stancomb-Wills (SW) ice tongue proper, surrounded by weaker ice mélange toward Lyddan Island, and to the south west toward Brunt Ice Shelf.

Third, and most relevant to the present study, the BSW system exhibits a varied distribution of rifts and faults. In particular, an extensive shear zone can be found separating the stagnant ice of Riiser-Larsen Ice Shelf to the east and the fast-flowing SW ice tongue. This shear zone is better described as a large crack about 150 km in length that decouples the flow of the SW ice tongue from Riiser-Larsen Ice Shelf. It runs through an ice mélange field at its north end, which defines the northeastern side of the SW ice tongue. In addition, two large cracks are found near the grounding line of SW, extending across-flow for up to 30 and 40 km respectively, as well as two large rifts near the ice front, which were identified in *Khazendar et al.* [2009] as critical in controlling the evolution of the BSW system. Indeed, both rifts are located at the almost exact center of rotation of the ice shelf system itself [*Hulbe et al.*, 2005]. These five rifts/cracks present a wide array of fracture and stress configurations which make the BSW system a valuable test bed for validation of an ice flow model.

Here we build on *Khazendar et al.* [2009] and their modeling work to include a representation of rifts and faults, especially along the northeastern edge of the SW ice tongue. Our model setup is essentially identical to that found in *Khazendar et al.* [2009] except when it relates to the inclusion of cracks (Figure 5) in the model domain. The five different locations referred to previously are identified as follows: crack 1 over the entire northeastern side of SW ice tongue, cracks 2 and 3 near the ice front, and cracks 4 and 5 near the grounding line. These crack locations are identified in *Khazendar et al.* [2009] as areas where the ice rigidity inversion fails to account for the discontinuity in observed surface velocities and coincide with areas of clear discontinuity in the radar amplitude image (Figure 4). The model domain is meshed at a resolution of 1 km, with an increase in resolution to 200 m in an area of 10 km^2 around the rupture tips of all five rifts, to account for the stress singularities exhibited in Figure 2. The threshold of 200 m was chosen as a

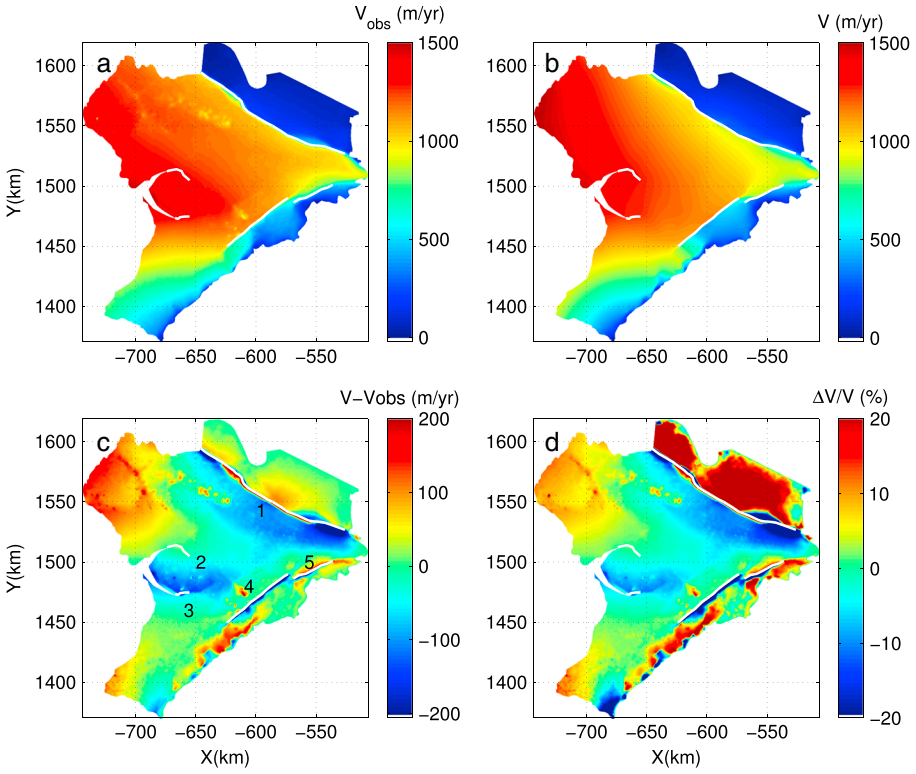

Figure 6. (a) InSAR derived surface velocities (m/yr). (b) Modeled surface velocity (m/yr), using the inverted ice rigidity and a forward model that includes a representation of rifts and faults. (c) Difference between modeled and observed velocity (m/yr). (d) Relative difference between modeled and observed velocity, in percent. Rifts and faults are traced in white on all four frames.

compromise between the need to model ice flow at a resolution equal to the ice thickness (dictated by the SSA formulation) and the need to account for stress singularities around rupture tips that are triggered by a change in the boundary conditions at the crack interface. This results in a mesh comprising 33,000 elements, with about 3600 elements used for the refinement around the rupture tips.

Model parameters are mapped onto the mesh using linear interpolation algorithms built into ISSM. Surface velocity is inferred from speckle tracking using RADARSAT-1 data acquired in 2000, with gaps filled using data from 1997. Resolution for the data is 50 m, with an accuracy of 10 m/yr. The grounding line position, which determines the southernmost boundary of the domain, is inferred from double interferometry using RADARSAT-1 (from 2000 for slower moving areas) and ERS 1/2 data (from 1996 for fast flow areas), at a precision of 100 m. The ice thickness, one of the main parameters for the ice flow model, is inferred using the GLAS/ICESat altimeter DEM of Antarctica from *DiMarzio et al.* [2007] assuming the ice is in hydrostatic equilibrium. To account for the presence of firn, we rely on the surface mass balance model for Antarctica from *van den Broeke* [2006, 2008], following *Khazendar et al.* [2009].

Several runs are carried out with this model setup. First, an inversion is performed to determine the distribution of B, starting from a uniform value of 500 kPa.yr$^{1/3}$, which corresponds to a temperature of 257 K as calibrated from *Paterson* [1994]. This temperature is 4 K warmer than the average surface temperature in the area [*Giovinetto et al.*, 1990] so as to account for the warmer thermal regime of an ice shelf. For comparison, an equivalent inversion is also performed for the same model without cracks. The results are presented in Figures 5, 6, and 8. Two additional experiments are then carried out to better understand the dynamics of the BSW system when the configuration of rifts and faults is modified. First, in the area between SW and Lyddan Island (shown in a black box in Figure 4), hereafter referred to as ice bridge, rift 1 is artificially closed and a forward model is run, to understand how this part of the ice shelf controls the flow of the SW tongue. Second, rifts 4 and 5 are artificially closed and a forward flow model is also run, to understand how the direction of the flow is modified and controlled at the grounding line. Results for both experiments are shown in Figure 10.

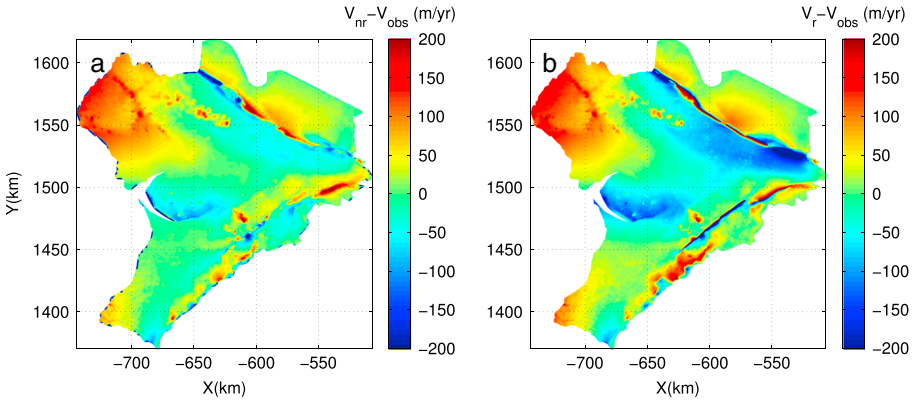

Figure 7. (a) Difference between modeled V_{nr} (m/yr) and observed surface velocity V_{obs} (m/yr) in the absence of explicit representation of rifts. (b) Difference between modeled V_r (m/yr) and observed surface velocity V_{obs} (m/yr) using the new model that explicitly captures the presence of rifts using cracks in the model mesh.

5. Results

5.1. Ice Rheology

The distribution of ice rigidity, along with the corresponding modeled surface velocity (Figures 5a and 5b) are similar to previous modeling results from *Khazendar et al.* [2009] when cracks were not represented. Bands of low ice rigidity are observed along Lyddan Island and near the grounding line of the BSW system, which corresponds to the observed cracks 3–5 on the radar amplitude image (Figure 4). This shows that the model inversion is efficient at locating areas where cracks are present. This is actually used, along with the radar amplitude image and the observed InSAR surface velocities, to accurately position the cracks. When these crack positions are set, and the inversion model is rerun, results are significantly different (Figures 5c and 5d), especially in the vicinity of fractures. Across cracks 1, 4, and 5, ice rheology is now uniform instead of rapidly varying. A more uniform ice shelf rigidity is indeed expected because the material make up of the ice shelf should be broadly the same in terms of temperature and fabrics on both sides of the crack since the ice has a common origin, whereas the prior inversions suggested a major contrast in ice shelf rheology as a result of cracking. One exception is near the rupture tip of cracks 4 and 5 where ice shelf rheology still varies strongly. The absence of similar features around rupture tips of cracks 1–3 suggests that this may be due to a problem in the positioning of crack tips 4 and 5, which leads to an over compensation of the stress singularities that are located in the wrong place. It could also be due to the fact that rifts 4 and 5 are the only cracks that are positioned across-flow, making them more prone to horizontal shearing. It could finally be due to the fact that the model does not account for the material heterogeneity that is observed to blunt rupture tips for active rifts [*Bassis et al.*, 2007].

Outside of the heavily cracked zones, the distribution of ice shelf rigidity in both runs (with and without cracks) exhibits the same lower values in areas of ice mélange identified in *Khazendar et al.* [2009]. These features are therefore robust and are not the result of limitations due to the absence of crack representation in the ice flow model. The same can be said for the modeled surface velocities, which in general do not vary significantly both with and without cracks (Figures 5a and 5c). Hence, standard inversions without fault/rift systems still capture the rate of ice flow deformation correctly. This is not true, however, in the immediate vicinity of rift and fault flanks, where ice shelf velocities are reproduced with improved fidelity in the new model, with however slight deterioration of the match far from the rifts (Figure 7). The new model produces, however, an ice shelf rheology which is more uniform across these cracks. This demonstrates that one of the major improvements resulting from the inclusion of cracks in an ice flow model is to infer a more realistic ice shelf rheology around cracks and also to reproduce ice shelf flow with greater fidelity along and at the rupture tip of cracks. One area where this could have strong implications is along the Caird Coast, where coupling between the floating ice and adjacent coastline appears to be quite weak, with low values of ice rigidity at approximately 200 kPa.yr$^{1/3}$. The introduction of cracks in this area would most probably modify the ice rigidity pattern (as the introduction of rifts 4 and 5 did), which in turn would have important consequences regarding the buttressing between Brunt Ice Shelf and Caird Coast. This area is of critical

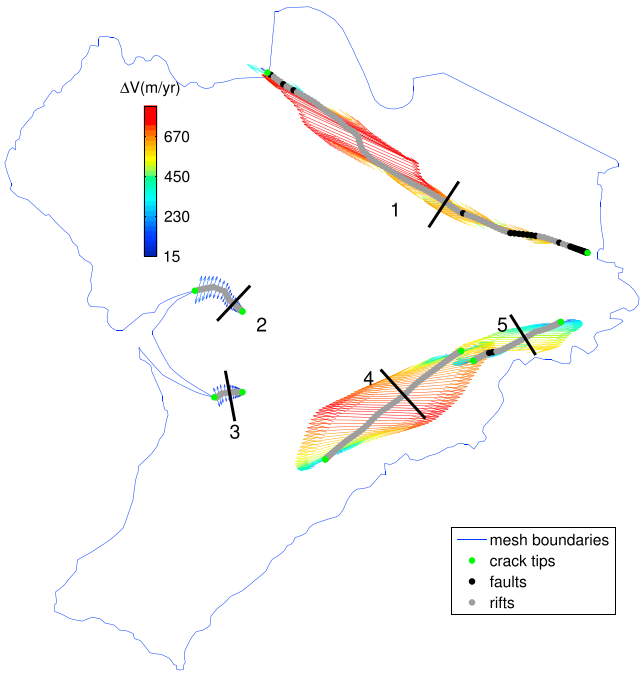

Figure 8. Velocity difference ΔV in m/yr across the five rifts and faults of the BSW system. Arrow color and length indicate the magnitude of the velocity difference in m/yr. Arrow directions indicate the direction of the velocity difference. Areas of contact between flanks are marked in black dots, whereas areas where flanks are opening (i.e., exhibiting positive ΔV) are marked in gray dots. For each crack, a profile is marked in black, perpendicular to the crack axis. These profiles are used in Figure 9 to compare across crack velocity differences against observations.

importance given the presence of the permanent Haley Station and the need to monitor the evolution and stability of this part of the BSW system.

Similar to the results in *Khazendar et al.* [2009], the modeled velocity matches surface velocity observations within ±10% (±50 m/yr) for the bulk of the SW tongue and the Brunt Ice Shelf (Figure 6). Near the ice front of the SW tongue, the velocities differ by ±13% (±200 m/yr), with the model overestimating the magnitude of the flow, despite the higher rigidity of the ice inferred in the inversion (Figure 5c). On the Riiser-Larsen Ice Shelf, the model overestimates the observed ice velocity by more than 20% (Figure 6d). This seemingly high value is however due to this ice shelf's low velocity, which makes relative differences to observed surface velocities inherently larger than for other parts of the BSW system. On the Brunt Ice Shelf, the rotation of the ice shelf mentioned by *Thomas* [1973b] and *Hulbe et al.* [2005] is well captured, and the center of rotation of the ice shelf is indeed located between rifts 2 and 3. Overall, the new model successfully replicates the modeled velocities across rifts, which is especially difficult given the gradients across each crack.

5.2. State of Contact/Opening

The new ice flow model provides information about the state of contact/opening of all the cracks in the domain (Figure 8) that was not readily available from analysis of the observed surface velocities. Cracks 2 and 3 exhibit very low rates of opening (30 m/yr on average along the entire crack lengths) compared to the other cracks, and none of the crack axis elements are in contact. Both cracks are therefore behaving as rifts that are almost inactive. Cracks 4 and 5 also behave as rifts, with however much higher rates of opening, 700 and 450 m/yr, respectively. These rates are almost on par with the background ice shelf velocity and compare well with observed rates of opening from InSAR (Figure 9). Indeed, the bulk of the ice acceleration observed for the SW ice tongue occurs across rifts 4 and 5. These rifts are therefore critical in characterizing ice flow. Downstream of rift 4 for example, acceleration along flow is much lower (Figures 6a and 6b), hinting at a system where tabular plates undergo creep deformation but where a significant part of the total deformation is due to the displacement along the boundaries of such plates, near shear margins, and across individual rifts.

East of SW ice tongue, crack 1 behaves in a very different manner. Figure 8 clearly shows a mixed rift/fault system, with contact occurring near the grounding line, 30 km from the grounding line, and 10 km from the ice front. Velocities along this crack are essentially tangential to the crack axis, which is expected when contact occurs, and the normal velocity differential is nil (due to the condition of non-interpenetration). Particularly relevant to the overall stability of the SW ice tongue is the presence of a contact area 10 km from the ice front. This area links SW and Lyddan Island in a band of what appears to be thicker and more homogeneous ice (see Figure 4, black box). It is the last point of contact between Riiser-Larsen Ice Shelf and the SW ice tongue, and it is located 80 km downstream of the next point of contact for crack 1. This ice bridge is captured by the model, though the exact location of it in the radar backscatter image (Figure 4) is further away from the ice front and less extensive (1–2 km long versus the modeled 20 km long). Because

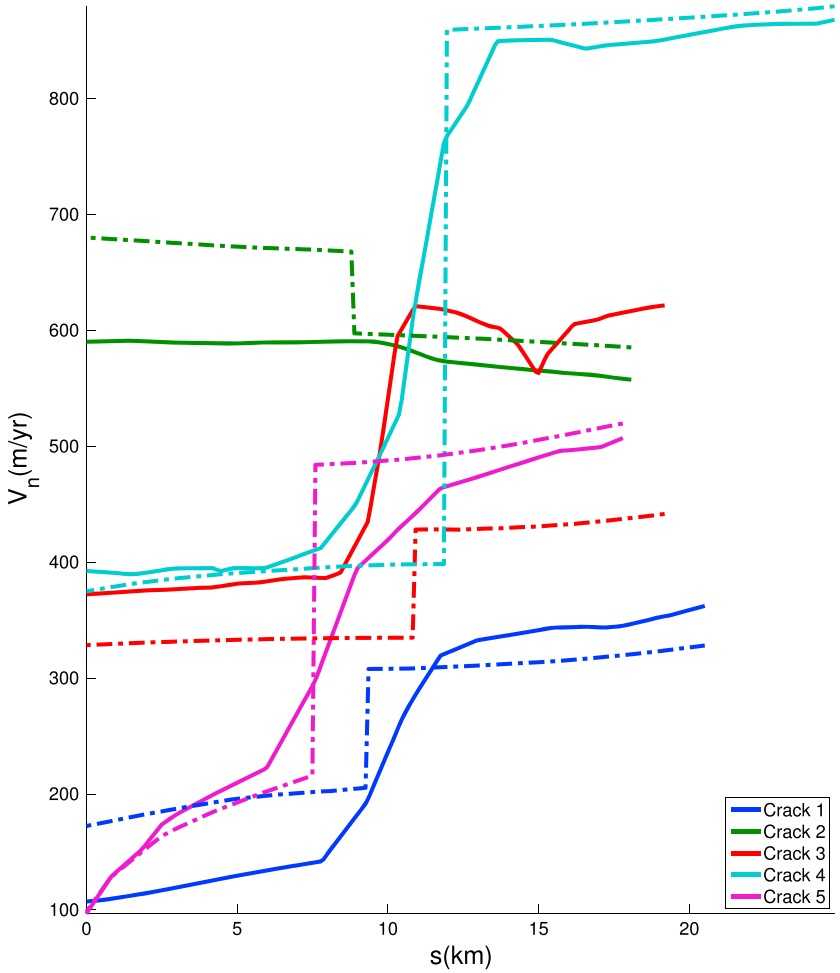

Figure 9. Observed (solid line) and modeled (dashed line) velocity in m/yr normal to all five cracks (along black profiles from Figure 8).

this bridge is located so far downstream from the nearest contact point on rift 1 and lies at the easternmost side of SW, it represents the only possible control point that could tie in the SW ice flow to the more stagnant ice of Lyddan Island.

To test the hypothesis that this ice bridge may play a critical role in controlling the dynamics of the BSW system, we artificially remove it and rerun the ice flow model accordingly. Results are shown in Figures 10a and 10b. A clear acceleration of approximately 300 m/yr is modeled, mainly downstream of the ice bridge. In addition, the SW ice tongue rotates counterclockwise on average 2–3°, up to 7.2° near the ice front. Southwest of rift 2, the situation is reversed, with the SW ice tongue as well as the Brunt Ice Shelf rotating clockwise on average 2°. These rotations have consequences for the state of all cracks. For rift/fault 1, the number of segments undergoing contact and friction increases, especially from the center of the crack to the grounding line. The almost entirety of the crack is a fault, with only small segments opening near the grounding line, and of course near the ice bridge. For rifts 2 and 3, the situation is interesting in that rift 2 undergoes a decrease in opening rate, while rift 3 undergoes an increase. Rift 2, in particular, appears to be at the transition zone between a counterclockwise rotating SW ice tongue, and a clockwise rotating Brunt Ice Shelf. For rifts 4 and 5, the situation is more stable, with both rifts seeing only a slight increase in the opening rate. The rupture of the ice bridge creates a realignment of the flow lines which is particularly important on the SW ice tongue near the ice front, where the new flow lines are rotated clockwise, opposite the general counterclockwise rotation of the SW ice tongue, as a direct result of the change in velocity field, with tensile strain rates reorienting away from Lyddan Island.

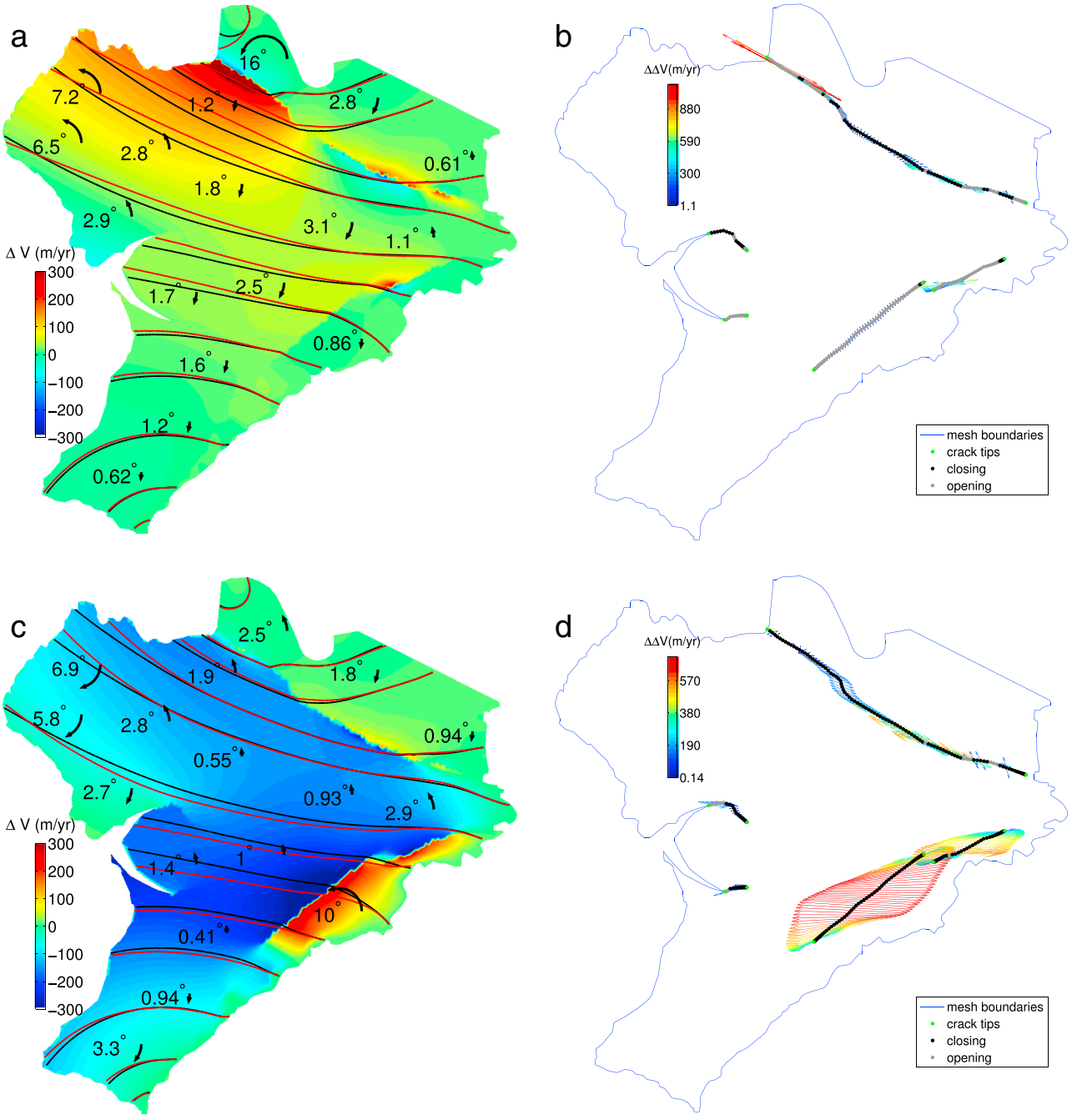

Figure 10. (a) Difference ΔV in modeled velocity (in m/yr) when the Lyddan Island ice bridge is artificially removed. Black lines represent flowlines prior to removal of the ice bridge. Red lines represent the same flowlines after removal of the ice bridge. Curved arrows with values in degrees indicate the local value of the rotation of the ice shelf induced by the removal of the ice bridge. (b) Corresponding modifications in contact across flanks of all five rifts. Locations marked with black dots correspond to decreased opening of the rifts, and locations marked in gray correspond to increased opening of the rifts. The arrows indicate the direction and magnitude (color coded) of the difference in velocity differentials ($\Delta\Delta V$, in m/yr) across rifts between the model with and without the ice bridge. (c) Difference ΔV in modeled velocity (in m/yr) when rifts 4 and 5 are artificially closed. Black lines represent flowlines prior to closing of rifts 4 and 5, red lines represent the same flowlines after closing of rifts 4 and 5. Curved arrows with values in degrees indicate the local value of the rotation of the ice shelf induced by the closing of the two rifts. (d) Corresponding modifications in contact across flanks of all five rifts. Locations marked with black dots correspond to decreased opening of the rifts, and locations marked in gray correspond to increased opening of the rifts. The arrows indicate the direction and magnitude (color coded) of the difference in velocity differentials ($\Delta\Delta V$, in m/yr) across rifts between the model that closes rifts 4 and 5, and the model that leaves them open.

To better understand how the rifts parallel to the grounding line may impact the dynamics of the BSW system, we carry out another experiment, in which rifts 4 and 5 are artificially closed. This results in an ice shelf wide slowdown of approximately 300 m/yr (Figure 10). The slowdown is most pronounced downstream of rift 4, with a corresponding acceleration of the ice upstream of rifts 4 and 5 due to entrainment of the ice from tensional stresses now sustainable by both cracks. In terms of rotation, the SW ice tongue now undergoes a clockwise rotation of approximately 6° near the ice front, and a counterclockwise rotation of approximately 1° upstream near the grounding line. Brunt Ice Shelf also rotates clockwise on average 1°, with peaks at 3.3° near Halley station. This results in flow lines that are now rotated counterclockwise, especially toward the Brunt Ice Shelf. For rifts 2, 3, and fault/rift 1, a general decrease in the opening rate occurs along with an increase in the amount of segments that undergo contact and friction. The rotation of the ice shelf upon closing of rifts 4 and 5 increases shearing along Lyddan Island, which participates in the slow down, and explains why the latter is generalized across the ice shelf.

6. Discussion

The new model captures the mechanics of contact and friction while at the same time improving inversion results of ice rigidity and the quality of model fitting near rupture zones. It also removes unrealistic rheology patterns obtained from inversions that are based on the assumption of a continuous domain. It improves our characterization of ice flow dynamics not only by providing a more realistic description of ice properties but also by highlighting areas of ice shelf rupture that matter to the entire ice shelf flow. Here the ice bridge between Lyddan Island and the SW ice tongue is an area that would have been difficult to isolate from an examination of backscatter images or ice velocity data alone. This zone is indicated by the inversion as an area of contact and friction. If the frictional forces that maintain this fault system in contact are removed, it leads to an acceleration of the ice shelf and a complex pattern of rotation which redistributes stresses as well as modifies the opening and/or closing rates of rifts and faults across the entire domain. If this ice bridge were to rupture and heal periodically, this could induce a periodic modification of the flow lines across the ice shelf, which would explain the "relict" flow stripes observed across the ice shelf (Figure 4) and first identified in *Wuite and Jezek* [2009]. Flow line reorientation would not be due to a thinning and associated grounding line migration as suggested in the latter study but rather to a modification of contact and frictional stresses on the most important shear zone of the BSW system.

Our results were tested for different initial values of ice rigidity B (ranging from 200 to 800 kPa $yr^{1/3}$) and showed the same robustness as that found in *Khazendar et al.* [2009]. In addition, several values of ν, the friction parameter, were tested, to understand the sensitivity of the model results to the friction coefficient. Results were very similar for a friction parameter ranging from 10^6 to 10^{14} kPa yr/m, showing little sensitivity. This can probably be explained by the fact that crack 1, where most of the friction occurs, is heavily kinked. Indeed, as evidenced in *MacAyeal et al.* [2003], such kinks tend to concentrate stress constraints and to control the overall pattern of friction, creating areas of no slip regardless of the value of the friction coefficient. It can also be attributed to the largely heterogeneous nature of the fabric of the BSW system, which can therefore accommodate large variations in friction without substantial impact on the stress regime.

The results of our second experiment indicate that a redistribution of stresses would also arise from healing of rifts 4 and 5 near the grounding line, with a rotation opposite that observed for the rupture of the ice bridge near Lyddan Island. This suggests that rifts near the grounding line are critical to understanding the dynamics of the BSW ice flow. The results also tend to confirm the hypothesis raised in *Khazendar et al.* [2009] that rift 2 might become unstable. Indeed, in both studies (removal of the ice bridge and healing of rifts at the grounding line), rift 2 is at the center of rotation of the BSW system, with the Eastern flank rotating synchronously with the SW ice tongue and the Western flank rotating synchronously with the Brunt Ice Shelf.

Both experiments present us with an interesting scenario in which strengthening of the ice bridge and healing of rifts at the grounding line decelerates the BSW system, while increasing shearing along crack 1 from the ice front to the grounding line. Weakening of the ice bridge and of the grounding line rifts, on the contrary, increases the BSW ice velocity, while weakening the shearing along crack 1 and destabilizing rift 2. Such weakening and strengthening would depend on the strength of the mélange present inside the rifts, its thickness, and the fabric of it.

Factors that can influence ice mélange can be atmospheric in nature, with cold air ponding responsible for thickening, as well as debris and wind-driven snow falling into the rifts. On the bottom side, accretion and melting of ice can be significant [*Khazendar and Jenkins*, 2003], forced by the underlying ocean circulation and the thermal regime of the ice shelf. As shown in *Thoma et al.* [2006, 2010], penetration of warm CDW water is possible up to the ice shelf, as the continental shelf is not wide in this area. Here we suggest that CDW penetration could be one of the regulating mechanisms controlling ice flow dynamics, by directly warming or cooling the underside of the ice shelf, especially along Lyddan Island and at the grounding line of SW ice tongue, hence modifying the thickness of the mélange present inside the rifts and consequently impacting the state of stress/contact of the entire ice shelf.

Our model does not simulate crack propagation, which as hypothesized in *Weertman* [1973, 1980], *van der Veen* [1998], *Rist et al.* [1999, 2002], *Plate et al.* [2012], and as observed in *Fricker et al.* [2005], and *Bassis et al.* [2005, 2007, 2008] on the rifts of the Amery Ice Shelf, is controlled by the elastic stress regime at the rupture tip. However, propagation models for rifts and faults are preconditioned by the creep stress distribution, which is then applied as a load to the linear elastic stress regime near the rupture tip [*van der Veen*, 1998; *Larour et al.*, 2004; *Hulbe et al.*, 2010; *Plate et al.*, 2012]. As such, our model is well suited for this type of loading, as it takes into account the presence of cracks and the way they impact the background stress of the ice shelf. In models such as *van der Veen* [1998] or *Plate et al.* [2012], the longitudinal stress applied to the rift flanks is taken equal to the background stress in which the crack is propagating. Such background stresses should therefore take into account the presence of the crack itself, which our model does. If used with such LEFM models, our ice flow model should yield better rates of propagation. In addition, our model best fits observations by inverting ice rigidity using an adjoint-based optimization. This again ensures that the background longitudinal stress is realistic. Finally, our model is capable of capturing the effect of multiple rifts and faults on the general flow of the ice shelf, ensuring that computed propagation rates fully account for the presence of multiple rifts, which as shown in *Weertman* [1973] and *van der Veen* [1998], can be a major source of background stress reduction through shielding between adjacent cracks. Overall, by better representing local background longitudinal stresses around rifts and faults, our model will significantly improve knowledge of the forcing applied to propagation models, which in turn will yield better estimates of how much the presence of cracks destabilizes an ice shelf and what drives the complex feedback between propagating cracks and ice flow dynamics.

7. Conclusions

We present a new ice flow model, capable of capturing the physics of rifted and faulted ice shelves. Inversions using this model result in improved distributions of ice shelf rigidity, especially in the immediate vicinity of rifts and faults. Its application to the BSW system improves the characterization of the rigidity of this strongly fractured ice shelf and highlights areas that are likely to trigger ice flow changes. Furthermore, this model is capable of quantifying the amount and the manner in which ice shelf flow is perturbed when contact/friction is modified at critical rupture points. It also improves our knowledge of how the presence of cracks impacts the local background longitudinal stress of the ice shelf, hence affecting propagation rates of active rifts and faults, and the overall stability of the ice shelf. Our approach is not limited to the BSW system. There are many similar ice shelves in Antarctica sharing common features, in particular, the presence of multiple faults and rifts. We expect this type of modeling to be relevant to other ice shelves such as Larsen B and C, Pine Island, and Thwaites ice shelves, among others, all ice shelves that exhibit complex distributions of cracks, rifts, and fault zones, which interact with the background ice flow dynamics in a complex way that the model presented here quantifies.

Acknowledgments

This work was supported by grants from NASA's Cryosphere Sciences Program (E.L., A.K., M.M., and E.R.) as well as funding from the Modeling, Analysis and Prediction Program (MAP, E.L., and H.S.) and funding from the President's and Director's Fund Program (E.L.). C.B. was supported by an appointment to the NASA Postdoctoral Program at the Jet Propulsion Laboratory, administered by Oak Ridge Associated Universities through a contract with NASA followed by an appointment to the Jet Propulsion Laboratory / California Institute of Technology Postdoctoral Program. This work was performed at the Jet Propulsion Laboratory, California Institute of Technology, under a contract with the National Aeronautics and Space Administration, and at the University of California, Irvine, Department of Earth System Science. The RADARSAT-1, ERS 1/2 data sets used in this study, along with the GLAS/ICESat altimeter DEM of Antarctica can be found at the NASA Distributed Active Archive Center at the National Snow and Ice Data Center, Boulder, Colorado, USA. We want to also thank Michiel van den Broeke for the surface mass balance model of Antarctica used in this study.

References

Banwell, A. F., D. R. MacAyeal, and O. V. Sergienko (2013), Breakup of the Larsen B ice shelf triggered by chain reaction drainage of supraglacial lakes, *Geophys. Res. Lett.*, *40*, 5872–5876, doi:10.1002/2013GL057694.

Bassis, J., R. Coleman, H. Fricker, and J. Minster (2005), Episodic propagation of a rift on the Amery Ice Shelf, East Antarctica, *Geophys. Res. Lett.*, *32*, L06502, doi:10.1029/2004GL022048.

Bassis, J. N., H. A. Fricker, R. Coleman, Y. Bock, J. Behrens, D. Darnell, M. Okal, and J.-B. Minster (2007), Seismicity and deformation associated with ice-shelf rift propagation, *J. Glaciol.*, *53*, 523–536.

Bassis, J. N., H. A. Fricker, R. Coleman, and J.-B. Minster (2008), An investigation into the forces that drive ice-shelf rift propagation on the Amery Ice Shelf, East Antarctica, *J. Glaciol.*, *54*, 17–27.

Borstad, C. P., A. Khazendar, E. Larour, M. Morlighem, E. Rignot, M. P. Schodlok, and H. Seroussi (2012), A damage mechanics assessment of the Larsen B ice shelf prior to collapse: Toward a physically-based calving law, *Geophys. Res. Lett.*, *39*, L18502, doi:10.1029/2012GL053317.

Borstad, C. P., E. Rignot, J. Mouginot, and M. P. Schodlok (2013), Creep deformation and buttressing capacity of damaged ice shelves: Theory and application to Larsen C ice shelf, *The Cryosphere*, *7*, 1931–1947.

Courant, R. (1943), Variational methods for the solution of problems of equilibrium and vibrations, *Bull. Am. Math. Soc.*, *49*, 1–23.

De Angelis, H., and P. Skvarca (2003), Glacier surge after ice shelf collapse, *Science*, *299*, 1560–1562.

DiMarzio, J., A. Brenner, R. Schutz, C. A. Shuman, and H. J. Zwally (2007), *Glas/ICESat 500 m Laser Altimetry Digital Elevation Model of Antarctica*, NASA Distributed Active Archive Center at the National Snow and Ice Data Center. Digital media, Boulder, Colo.

Fricker, H., N. Young, R. Coleman, J. Bassis, and J. Minster (2005), Multi-year monitoring of rift propagation on the Amery Ice Shelf, East Antarctica, *Geophys. Res. Lett.*, *32*, L02502, doi:10.1029/2004GL021036.

Giovinetto, M., N. Waters, and C. Bentley (1990), Dependence of Antarctic surface mass balance on temperature, elevation, and distance to open ocean, *J. Geophys. Res.*, *95*, 3517–3531.

Glen, J. (1955), The creep of polycrystalline ice, *Proc. R. Soc. A*, *228*, 519–538.

Hulbe, C., R. Johnston, I. Joughin, and T. Scambos (2005), Marine ice modification of fringing ice shelf flow, *Arct. Antarct. Alp. Res.*, *37*, 323–330.

Hulbe, C., C. LeDoux, and K. Cruikshank (2010), Propagation of long fractures in the Ronne Ice Shelf, Antarctica, investigated using a numerical model of fracture propagation, *J. Glaciol.*, *56*, 459–472.

Hulbe, C. L., T. A. Scambos, and T. Youngberg (2008), Patterns of glacier response to disintegration of the Larsen B ice shelf, Antarctic Peninsula, *Global Planet. Change*, *63*, 1–8, doi:10.1016/j.gloplacha.2008.04.001.

Humbert, A., T. Kleiner, C.-O. Mohrholz, C. Oelke, R. Greve, and M. A. Lange (2009), A comparative modeling study of the Brunt Ice Shelf/Stancomb-Wills Ice Tongue system, East Antarctica, *J. Glaciol.*, *55*, 53–65.

Hutchinson, J. (1968), Singular behaviour at end of a tensile crack in a hardening material, *J. Mech. Phys. Solids*, *16*, 13–81.

Jezek, K., and R. P. Team (2002), *Ramp AMM-1 SAR Image Mosaic of Antarctica, Version 2*, National Snow and Ice Data Center, Boulder, Colo.

Khazendar, A., and A. Jenkins (2003), A model of marine ice formation within Antarctic ice shelf rifts, *J. Geophys. Res.*, *108*, 3235, doi:10.1029/2002JC001673.

Khazendar, A., E. Rignot, and E. Larour (2007), Larsen B Ice Shelf rheology preceding its disintegration inferred by a control method, *Geophys. Res. Lett.*, *34*, L19503, doi:10.1029/2007GL030980.

Khazendar, A., E. Rignot, and E. Larour (2009), Roles of marine ice, rheology, and fracture in the flow and stability of the Brunt/Stancomb-Wills Ice Shelf, *J. Geophys. Res.*, *114*, F04007, doi:10.1029/2008JF001124.

Khazendar, A., E. Rignot, and E. Larour (2011), Acceleration and spatial rheology of Larsen C ice shelf, Antarctic Peninsula, *38*, L09502, doi:10.1029/2011GL046775.

King, J. (1993), Control of near-surface winds over an Antarctic ice shelf, *J. Geophys. Res.*, *98*, 12949–12953, doi:10.1029/92JD02425.

Larour, E. (2005), Modélisation numérique du comportement des banquises flottantes, validée par imagerie satellitaire, PhD thesis, Ecole Centrale Paris, Chatenay-Malabry, France.

Larour, E., E. Rignot, and D. Aubry (2004), Processes involved in the propagation of rifts near Hemmen ice rise, Ronne ice shelf, Antarctica, *J. Glaciol.*, *50*, 329–341.

Larour, E., E. Rignot, I. Joughin, and D. Aubry (2005), Rheology of the Ronne ice shelf, Antarctica, inferred from satellite radar interferometry data using an inverse control method, *Geophys. Res. Lett.*, *32*, L05503, doi:10.1029/2004GL021693.

Larour, E., H. Seroussi, M. Morlighem, and E. Rignot (2012), Continental scale, high order, high spatial resolution, ice sheet modeling using the Ice Sheet System Model (ISSM), *J. Geophys. Res.*, *117*, 1–20, doi:10.1029/2011JF002140.

MacAyeal, D. (1989), Large-scale ice flow over a viscous basal sediment: Theory and application to ice stream B, Antarctica, *J. Geophys. Res.*, *94*, 4071–4087.

MacAyeal, D. (1992), The basal stress distribution of ice stream E, Antarctica, inferred by control methods, *J. Geophys. Res.*, *97*, 595–603.

MacAyeal, D., E. Rignot, and C. Hulbe (1998), Ice-shelf dynamics near the front of the Filchner-Ronne ice shelf, Antarctica, revealed by SAR interferometry: Model/interferogram comparison, *J. Glaciol.*, *44*, 419–428.

MacAyeal, D. R., T. A. Scambos, C. L. Hulbe, and M. A. Fahnestock (2003), Catastrophic ice-shelf break-up by an ice-shelf-fragment-capsize mechanism, *J. Glaciol.*, *49*, 22–36.

Morland, L., and R. Zainuddin (1987), Plane and radial ice-shelf flow with prescribed temperature profile, in *Dynamics of the West Antarctica Ice Sheet. Proceedings of a Workshop Held in Utrecht, May 6-8, 1985*, vol. 4, edited by C. J. van der Veen and J. Oerlemans, pp. 117–140, D. Rediel, Dordrecht, Netherland.

Morlighem, M., E. Rignot, H. Seroussi, E. Larour, H. Ben Dhia, and D. Aubry (2010), Spatial patterns of basal drag inferred using control methods from a full-Stokes and simpler models for Pine Island Glacier, West Antarctica, *Geophys. Res. Lett.*, *37*, L14502, doi:10.1029/2010GL043853.

Paterson, W. (1994), *The Physics of Glaciers,* 3rd ed., Pergamon Press, Oxford, London, New York.

Plate, C., R. Müller, A. Humbert, and D. Gross (2012), Evaluation of the criticality of cracks in ice shelves using finite element simulations, *The Cryosphere*, *6*, 973–984.

Pritchard, H. D., and D. G. Vaughan (2007), Widespread acceleration of tidewater glaciers on the Antarctic Peninsula, *J. Geophys. Res.*, *112*, F03S29, doi:10.1029/2006JF000597.

Reist, A. (2005), Mathematical analysis and numerical simulation of the motion of a glacier, PhD thesis, Ecole Polytechnique Fédérale de Lausanne, Switzerland.

Renfrew, I., and P. Anderson (2002), The surface climatology of an ordinary katabatic wind regime in Coats Land, Antarctica, *Tellus A*, *54*, 463–484, Climate Conference 2001, Utrecht Univ, Utrecht, Netherlands, August 2001.

Renfrew, I., and P. Anderson (2006), Profiles of katabatic flow in summer and winter over Coats Land, Antarctica, *Q. J. R. Meteorol. Soc.*, *132*, 779–802.

Rice, J., and G. Rosengren (1968), Plane strain deformation near a crack top in a power-law hardening material, *J. Mech. Phys. Solids*, *16*, 1–12.

Rignot, E. (1998), Fast recession of a West Antarctic glacier, *Science*, *281*, 549–551.

Rignot, E., G. Casassa, P. Gogineni, W. Krabill, A. Rivera, and R. Thomas (2004), Accelerated ice discharge from the Antarctic Peninsula following the collapse of Larsen B ice shelf, *Geophys. Res. Lett.*, *31*, L18401, doi:10.1029/2004GL020697.

Rignot, E., G. Casassa, S. Gogineni, P. Kanagaratnam, W. Krabill, H. Pritchard, A. Rivera, R. Thomas, J. Turner, and D. Vaughan (2005), Recent ice loss from the Fleming and other glaciers, Wordie Bay, West Antarctic Peninsula, *Geophys. Res. Lett.*, *32*, L07502, doi:10.1029/2004GL021947.

Rist, M., P. Sammonds, S. Murrell, P. Meredith, C. Doake, H. Oerter, and K. Matsuki (1999), Experimental and theoretical fracture mechanics applied to Antarctic ice fracture and surface crevassing, *J. Geophys. Res.*, *104*, 2973–2987.
Rist, M., P. Sammonds, H. Oerter, and C. Doake (2002), Fracture of Antarctic shelf ice, *J. Geophys. Res.*, *107*(B1), ECV 2-1–ECV 2-13, doi:10.1029/2000JB000058.
Rott, H., W. Rack, P. Skvarca, and H. De Angelis (2002), Northern Larsen ice shelf, Antarctica: Further retreat after collapse, *Ann. Glaciol.*, *34*, 277–282.
Scambos, T., C. Hulbe, M. Fahnestock, and J. Bohlander (2000), The link between climate warming and break-up of ice shelves in the Antarctic Peninsula, *J. Glaciol.*, *46*, 516–530.
Scambos, T., J. Bohlander, C. Shuman, and P. Skvarca (2004), Glacier acceleration and thinning after ice shelf collapse in the Larsen B embayment, Antarctica, *Geophys. Res. Lett.*, *31*, L18402, doi:10.1029/2004GL020670.
Scambos, T., H. A. Fricker, C.-C. Liu, J. Bohlander, J. Fastook, A. Sargent, R. Massom, and A.-M. Wu (2009), Ice shelf disintegration by plate bending and hydro-fracture: Satellite observations and model results of the 2008 Wilkins ice shelf break-ups, *Earth Planet. Sci. Lett.*, *280*, 51–60.
Shepherd, A., D. Wingham, T. Payne, and P. Skvarca (2003), Larsen ice shelf has progressively thinned, *Science*, *302*, 856–859.
Simmons, D. (1986), Flow of the Brunt Ice Shelf, Antarctica, derived from Landsat images, 1974–85, *J. Glaciol.*, *32*, 252–254.
Simmons, D., and J. Rouse (1984), Accelerating flow of the Brunt Ice Shelf, Antarctica, *J. Glaciol.*, *30*, 377–380.
Smith, R. (1976), The application of fracture mechanics to the problem of crevasse penetration, *J. Glaciol.*, *17*, 223–228.
Thoma, M., K. Grosfeld, and M. A. Lange (2006), Impact of the Eastern Weddell ice shelves on water masses in the Eastern Weddell Sea, *J. Geophys. Res.*, *111*, C12010, doi:10.1029/2005JC003212.
Thoma, M., K. Grosfeld, K. Makinson, and M. A. Lange (2010), Modelling the impact of ocean warming on melting and water masses of ice shelves in the Eastern Weddell Sea, *Ocean Dyn.*, *60*, 479–489.
Thomas, R. H. (1973a), The creep of ice shelves: Theory, *J. Glaciol.*, *12*, 45–53.
Thomas, R. H. (1973b), The creep of ice shelves: Interpretation of observed behaviour, *J. Glaciol.*, *12*, 55–70.
van den Broeke, M. (2005), Strong surface melting preceded collapse of Antarctic Peninsula ice shelf, *Geophys. Res. Lett.*, *32*, L12815, doi:10.1029/2005GL023247.
van den Broeke, M. (2006), Towards quantifying the contribution of the Antarctic ice sheet to global sea level change, *J. Phys. IV*, *139*, 175–183.
van den Broeke, M. (2008), Depth and density of the Antarctic firn layer, *Arct. Antarct. Alp. Res.*, *40*, 432–438.
van der Veen, C. (1998), Fracture mechanics approach to penetration of bottom crevasses on glaciers, *Cold Reg. Sci. Technol.*, *27*, 213–223.
Vaughan, D. (1993), Relating the occurence of crevasses to surface strain rates, *J. Glaciol.*, *39*(132), 255–266.
Vieli, A., A. J. Payne, Z. Du, and A. Shepherd (2006), Numerical modelling and data assimilation of the Larsen B ice shelf, Antarctic Peninsula, *Philos. Trans R. Soc. A*, *364*, 1815–1839.
Vieli, A., A. J. Payne, A. Shepherd, and Z. Du (2007), Causes of pre-collapse changes of the Larsen B ice shelf: Numerical modelling and assimilation of satellite observations, *Earth Planet. Sci. Lett.*, *259*, 297–306.
Weertman, J. (1973), Can a water-filled crevasse reach the bottom surface of a glacier?, *IASH Publ.*, *95*, 139–145.
Weertman, J. (1980), Bottom crevasses, *J. Glaciol.*, *25*(91), 185–188.
Wriggers, P. (2002), *Computational Contact Mechanics*, John Wiley, New York.
Wuite, J., and K. C. Jezek (2009), Evidence of past fluctuations on Stancomb-Wills Ice Tongue, Antarctica, preserved by relict flow stripes, *J. Glaciol.*, *55*, 239–244.